Article:
Shi, Q, Shih, E-M, Rhodes, D et al. (2022) Bilayer WSe2 as a natural platform for interlayer exciton condensates in the strong coupling limit. Nature Nanotechnology, 17 (6). pp. 577-582. ISSN: 1748-3387

https://doi.org/10.1038/s41565-022-01104-5

Bilayer WSe_2 as a natural platform for interlayer exciton condensates in the strong coupling limit

Qianhui Shi,[1,2] En-Min Shih,[1,*] Daniel Rhodes,[3] Bumho Kim,[3] Katayun Barmak,[4] Kenji Watanabe,[5] Takashi Taniguchi,[6] Zlatko Papić,[7] Dmitry A. Abanin,[8] James Hone,[3] and Cory R. Dean[1]

[1]*Department of Physics, Columbia University, New York, NY, USA*
[2]*Department of Physics and Astronomy, University of California, Los Angeles, CA, USA*
[3]*Department of Mechanical Engineering, Columbia University, New York, NY, USA*
[4]*Department of Applied Physics and Applied Mathematics, Columbia University, New York, NY, USA*
[5]*Research Center for Functional Materials, National Institute for Materials Science, 1-1 Namiki, Tsukuba 305-0044, Japan*
[6]*International Center for Materials Nanoarchitectonics, National Institute for Materials Science, 1-1 Namiki, Tsukuba 305-0044, Japan*
[7]*School of Physics and Astronomy, University of Leeds, Leeds LS2 9JT, UK*
[8]*Department of Theoretical Physics, University of Geneva, 24 quai Ernest-Ansermet, 1211 Geneva, Switzerland*

(Dated: July 6, 2022)

Exciton condensates (EC) are macroscopic coherent states arising from condensation of electron-hole pairs [1]. Bilayer heterostructures, consisting of two-dimensional electron and hole layers separated by a tunnel barrier, provide a versatile platform to realize and study EC [2–4]. The tunnel barrier suppresses recombination yielding long-lived excitons [5–10]. However, this separation also reduces interlayer Coulomb interactions, limiting the exciton binding strength. Here, we report the observation of EC in naturally occurring 2H-stacked bilayer WSe_2. In this system, the intrinsic spin-valley structure suppresses interlayer tunneling even when the separation is reduced to the atomic limit, providing access to a previously unattainable regime of strong interlayer coupling. Using capacitance spectroscopy, we investigate magneto-EC, formed when partially filled Landau levels (LL) couple between the layers. We find that the strong-coupling EC show dramatically different behaviour compared with previous reports, including an unanticipated variation of EC robustness with the orbital number, and find evidence for a transition between two types of low-energy charged excitations. Our results provide a demonstration of tuning EC properties by varying the constituent single-particle wavefunctions.

Narrow-gap semiconductors or semi-metals were originally proposed as natural hosts for EC due to a spontaneous paring instability between the electrons and holes, provided that the Coulomb interaction between them exceeds the band gap [11]. Signatures of EC have been identified in several such candidate systems [12–16], though debates are still ongoing due to challenges to disentangle lattice-related effects [17, 18]. In another direction, EC have been explored in layered structures where electrons and holes are spatially confined to separate layers [2, 19–21]. These so-called spatially indirect excitons can be generated by either optical excitation or electrical gating [3, 10, 22]. The spatial separation of the electrons and holes inhibits recombination and therefore extends the exciton lifetime, making it possible to observe the EC under equilibrium conditions [10].

Quantum Hall bilayers provide a robust model platform to study the spatially indirect EC [4, 6–8]. In these systems, a heterostructure consisting of electrically-isolated parallel layers is exposed to a perpendicular magnetic field. Interlayer excitons can then form between partially filled LLs with filled (electron) states in one layer coupling to vacancy (hole) states in the other layer. A key advantage of this approach is that, within the flat LLs, kinetic energy is quenched and Coulomb interactions necessarily play a dominant role. Quantum Hall bilayers fabricated from GaAs double wells provided the first direct evidence of exciton superfluidity [6, 23], appearing when each layer was tuned to half filling of the lowest Landau level. More recently, superfluid EC have been studied in graphene heterostructures, consisting of two graphene layers separated by a boron nitride tunnel barrier, where increased flexibility in device architecture has expanded the accessible phase space [7, 8].

The EC phase diagram is determined by the interplay between the interlayer Coulomb attraction, $E_{inter} \propto 1/d$, where d is the layer separation, and intralayer Coulomb repulsion, $E_{intra} \propto 1/l_B$, where $l_B = \sqrt{\hbar/eB}$ is the magnetic length [6]. Whereas l_B can be widely varied with B, d is more restricted since it must be small enough to promote strong coupling between the layers, at the same time remaining large enough to suppress interlayer tunneling. In GaAs bilayers, $d > 10$ nm, and the EC are measurable only in the so-called weak coupling limit ($d/l_B \sim 1$) [6]. Recent efforts in graphene double layers demonstrated the ability to access the strong coupling regime ($d/l_B < 0.5$), by reducing the layer separation to just a few nanometers [24]. Owing to the inability to fur-

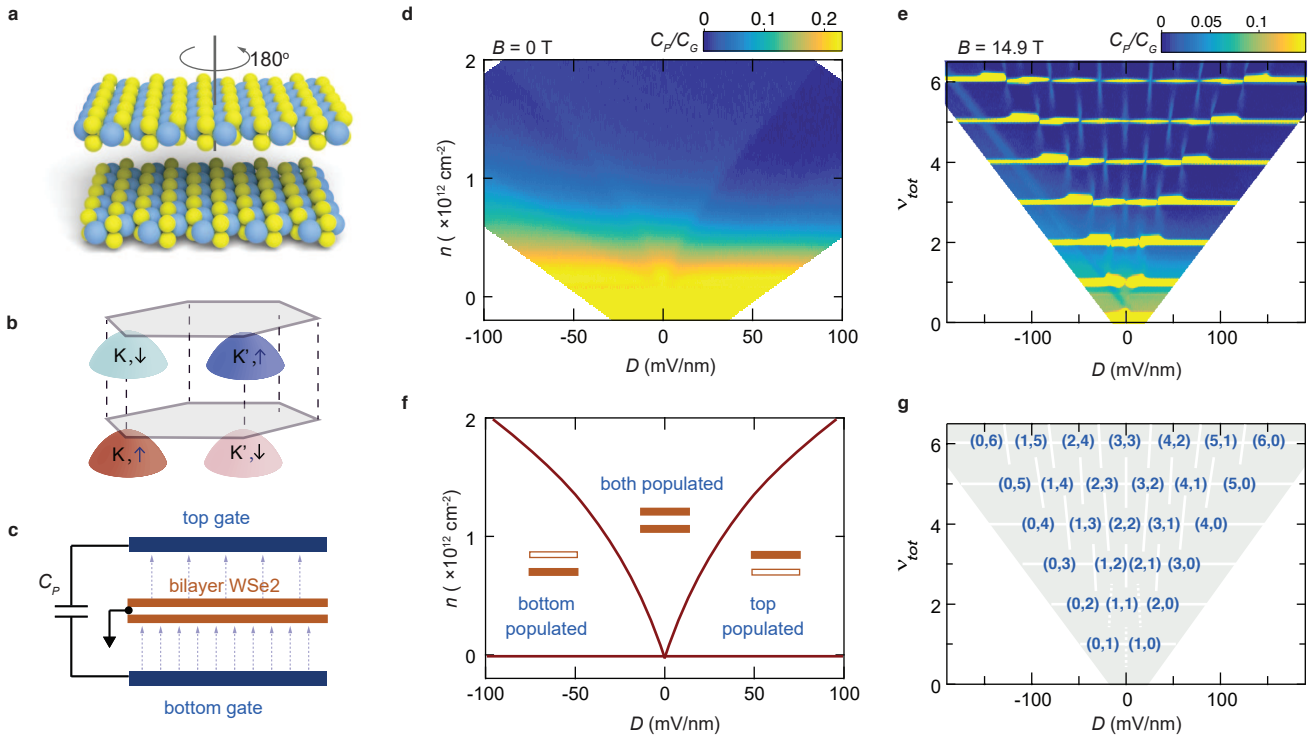

FIG. 1. **Independent layer population in bilayer WSe_2.** (a) Schematic of WSe_2 bilayer crystal structure. (b) Schematic illustration of the four flavors in the valence band in bilayer WSe_2. (c) Schematic illustration of the penetration capacitance measurements. (d) Penetration capacitance of bilayer WSe_2 measured at $B = 0$ and $T = 0.3$ K, versus ν_{tot} and D. (e) Schematic phase diagram of layer population according to features in (c). (f) Penetration capacitance measured at $B = 14.9$ T and $T = 0.3$ K, versus ν_{tot} and D. (g) Schematic illustration of features shown in (e). The filling factors in each layers are marked as (ν_T, ν_B) for the integer gaps.

ther reduce d without introducing appreciable tunneling, the regime of extreme strong coupling remains almost completely unexplored [25].

Here we identify the natural bilayer WSe_2 as a system that provides a unique opportunity to realize EC in the previously inaccessible regime of extreme strong interlayer coupling. In this case, interlayer tunneling is naturally suppressed via a spin-blocking mechanism, due to combination of the spin-valley locking and stacking order. This eliminates the need to insert a physical tunnel barrier, thereby allowing the layer separation to be reduced to the atomic limit. Previously, in the weak coupling regime, EC has only been observed in the lowest LL ($n = 0$). Remarkably, here we observe EC in higher LLs up to $n = 6$. Our data indicates that in the strong coupling regime the low-energy charged excitations have a different nature in different LLs, rendering the EC more robust in high LLs than in the lowest LL.

Fig. 1(a) shows a schematic of the crystal structure for 2H-stacked bilayer WSe_2, consisting of two monolayers rotated 180 degrees to each other. In Fig.1(b) we sketch the low-energy valence bands, with the valley and spin indices indicated. Strong spin-orbit coupling gives rise to spin-valley locking within each layer, with the K and K' valleys oppositely spin-polarized. Due to the stacking order, carriers residing in the same valley have opposite spin in the two layers, leading to strongly suppressed interlayer tunneling [26–30] (also see SI.1).

In our experiment, we measure the penetration capacitance C_P, illustrated in Fig.1(c), which has proven to be an effective probe that circumvents non-ideal electrical contact and disorder effects in 2D semiconducting transition metal dichalcogenides [31]. While C_P reflects the inverse compressibility of a monolayer system, for a multi-layer system it has an additional contribution from the polarizability. The penetration capacitance normalized to the geometric capacitance between the top and bottom gates (C_G) can be written as [32, 33],

$$\frac{C_P}{C_G} = \frac{2c\partial\mu/\partial n}{e^2 + 2c\partial\mu/\partial n} + \frac{ec}{4\epsilon_0 c_0}\frac{\partial\Delta n}{\partial D}. \quad (1)$$

Here, c is the capacitance (per unit area) between the bilayer WSe_2 and the gates, c_0 is the interlayer capacitance (per unit area) of the bilayer WSe_2, $\partial\mu/\partial n$ is the inverse electronic compressibility where μ is the chemical potential and n is the total carrier density, $\Delta n = n_T - n_B$ is the carrier density imbalance of the two layers, and $D = c(V_B - V_T)/2\epsilon_0$ is the displacement electric field

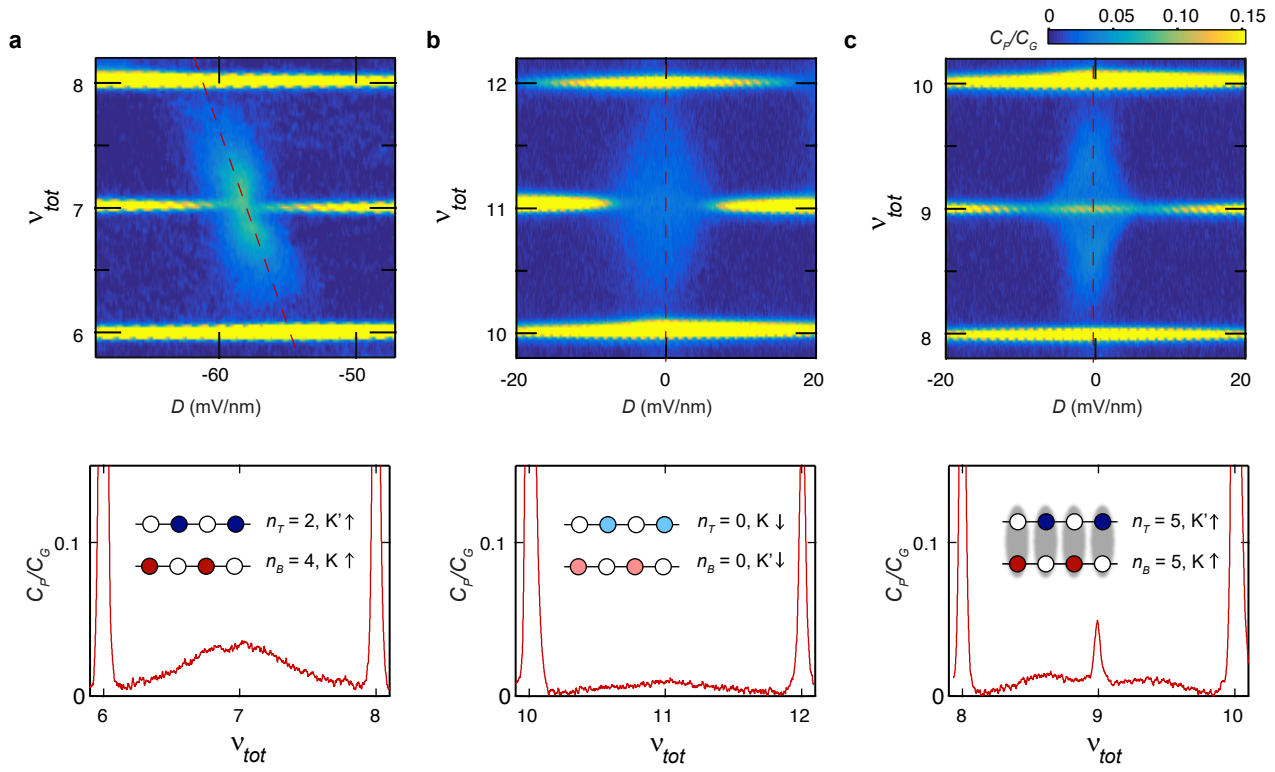

FIG. 2. **EC formation and gap opening at LL crossings.** (a-c) Penetration capacitance versus total filling factor ν_{tot} and displacement field D at $B = 14.9$ T around several LL crossings. The bottom panel are linecut along the red dashed line in the top panel, which tracks equal topmost LL population in the two layers. The insets of the bottom panel illustrate the orbital, spin and valley indices.

on the bilayer. The two terms in the right hand side of Eq. (1) correspond to "incompressibility" and "polarizability" contributions, respectively; a large signal in C_P indicates that the system is either incompressible or highly polarizable.

We first demonstrate that we can achieve layer-selective population in bilayer WSe_2 through gate control. In Fig.1(d) we plot the penetration capacitance versus the displacement field and total density. For a fixed carrier density, the electron polarization can be tuned through three regions, corresponding to the bottom, top or both layer populated. The transition from full layer polarization to partial polarization is visible as a step in the C_P/C_G, owing to a finite polarizability contribution in the latter. This step follows a curved shape that defines the polarization boundaries in the space of D vs n (see SI.3).

The layer-selective population becomes more apparent as a perpendicular magnetic field is applied, and the energy spectrum splits into discrete LLs. In Fig.1(e) we plot C_P/C_G as a function of D and total filling factor $\nu_{tot} = \nu_T + \nu_B$, where ν_T and ν_B are the top and bottom layer LL filling fractions, respectively. Horizontal features are observed at integer values of ν_{tot}. These peaks in C_P indicate incompressibility when the Fermi level is within an integer quantum Hall (IQH) gap. In the bilayer populated region, each feature is interrupted by exactly ν_{tot} vertical features, as schematically illustrated in Fig.1(g). This is consistent with discrete filling of the LLs in each layer: with increasing D, ν_T increases step-wise from 0 to ν_{tot}, and ν_B decreases from ν_{tot} to 0. Interlayer charge transfer is allowed only when the displacement field induces crossings of LLs in the two layers. At the crossing points, the bilayer system manifests increased polarizability at both integer and non-integer fillings, giving rise to the vertical features in Fig.1(e) (see SI.4 for more details).

Next, we examine the penetration capacitance at the LL crossings. Fig. 2 shows representative examples of the three types of behaviour we observe. At the center of each $\nu_{tot} - D$ map, a light blue diamond area demarcates the region where both layers host fractional filling factors and the system has finite polarizability. Fig.2(a) and (b) show two examples where the gap closes, leading to a disappearance of the sharp horizontal feature at integer ν_{tot}. This behavior is seen for most LL crossings, and is consistent with the single-particle picture of LL crossings - the bilayer system is compressible since both layers are partially filled. The gap closing in (a) and (b) also confirms the suppression of interlayer tunneling, which would otherwise induce LL anti-crossings and preserve the gap. Fig.2(c), on the contrary, demonstrates an ex-

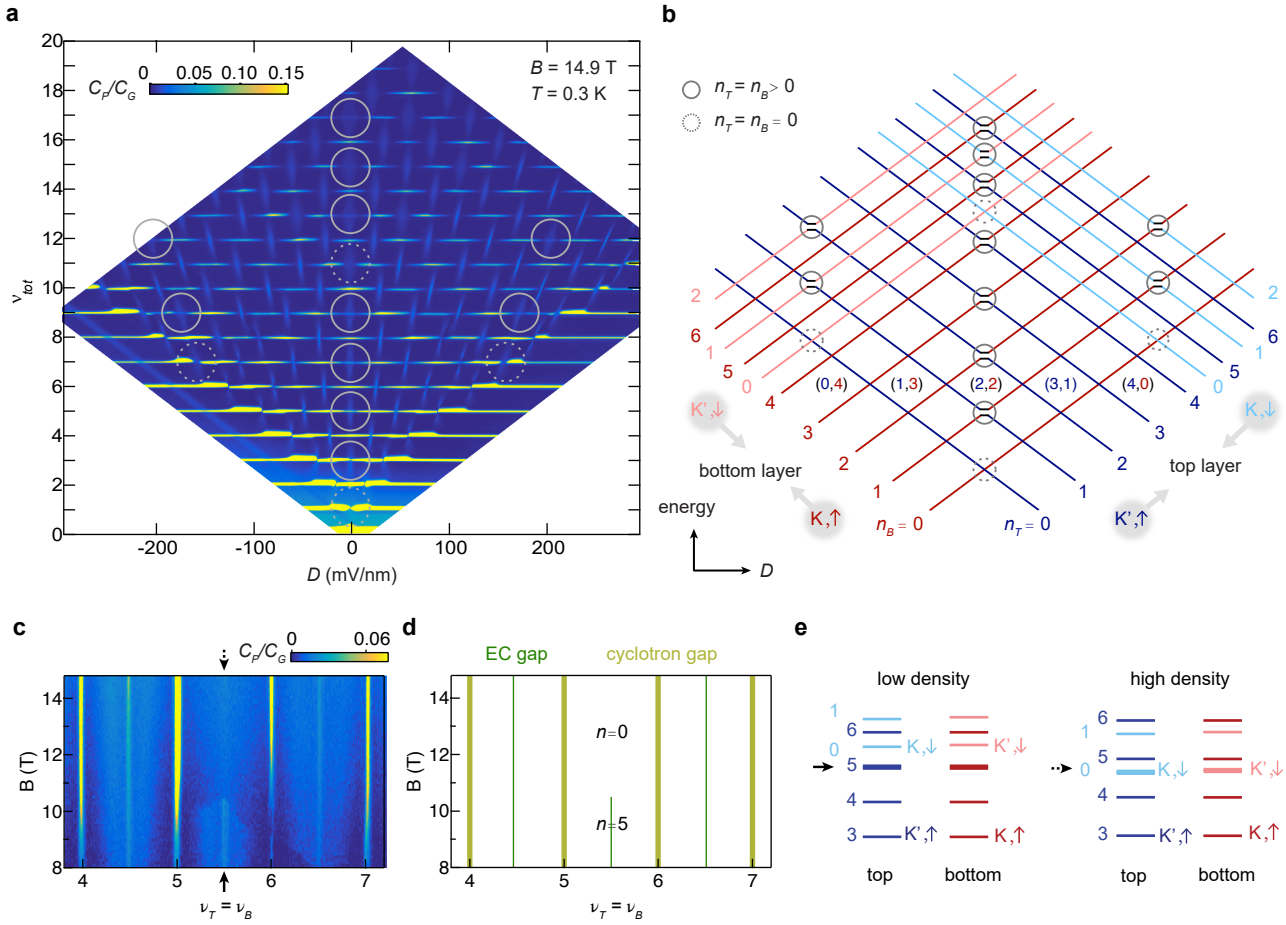

FIG. 3. **Conditions for exciton condensate formation.** (a) Penetration capacitance versus total filling factor ν_{tot} and displacement field D at $B = 14.9$ T. Solid (dotted) circles mark the crossings where the two LLs have the same orbital number $n = n_T = n_B > 0$ ($n = n_T = n_B = 0$). (b) Schematic LLs diagram. As D is varied, LLs in the bottom layer increases in energy and those of the top layer increases, giving rise to LL crossings. Each layer hosts LLs from two spin branches, with a large spin-splitting energy several times of the cyclotron gap. LLs from 4 different flavors are marked by different colors and the orbital number is also marked. (c) Penetration capacitance at the layer balanced condition $\nu_T = \nu_B$, as a function of the filling factor and magnetic field. (d) Schematic illustration according to (c), with yellow lines standing for the IQH gap, and the green lines standing for the EC gap. Orbital numbers are marked for different regions for $\nu_T = \nu_B = 5.5$. (e)Cartoon illustrating the LL structure at low and high densities respectively. The black arrow points to the Fermi level at $\nu = 5.5$, where active LLs have orbital number $n = 5$ and $n = 0$, respectively.

ample where the gap persists throughout the fractional filling region. The two scenarios regarding the presence or absence of a gap at the level crossings are clearly distinguishable in linecuts taken through the center of the fractional-filling region (bottom panels): a sharp spike in C_P is seen at integer ν_{tot} for (c), but is absent in (a) and (b). Having established that the two layers are tunnel-decoupled, we interpret the incompressible states while both layers are partially filled in (c) as interlayer correlated states, *i.e.* exciton condensates.

In Fig.3(a) we plot C_P as a function of ν_{tot} and D over a broad range, and mark the location of EC by solid circles using the criteria established in Fig.2. Remarkably, EC appear for a large range of LLs - far beyond what has been previously observed - both where the layers are balanced (around $D = 0$) and where they are very imbalanced (at large D). Fig.3(b) shows the corresponding schematic LL diagram, which identifies the LL orbital and spin/valley indices (see SI.2). We note first that all of the EC correspond to states with matched orbital number n. The series of EC at $D = 0$ (with Fig.2(c) as an example) corresponds to the crossings of two LLs with the same orbital number and spin indices but different valley index; while those at finite D correspond to matched orbital numbers and valley indices but different spins (see SI.5).

Our observations indicate that EC formation requires the orbital wavefunctions to match, but is independent of the spin/valley degree of freedom. Likewise, our Hartree-Fock and numerical calculations suggest that formation of EC, characterized by a good overlap with the Halperin (111) wavefunction and a gapless neutral mode, only ap-

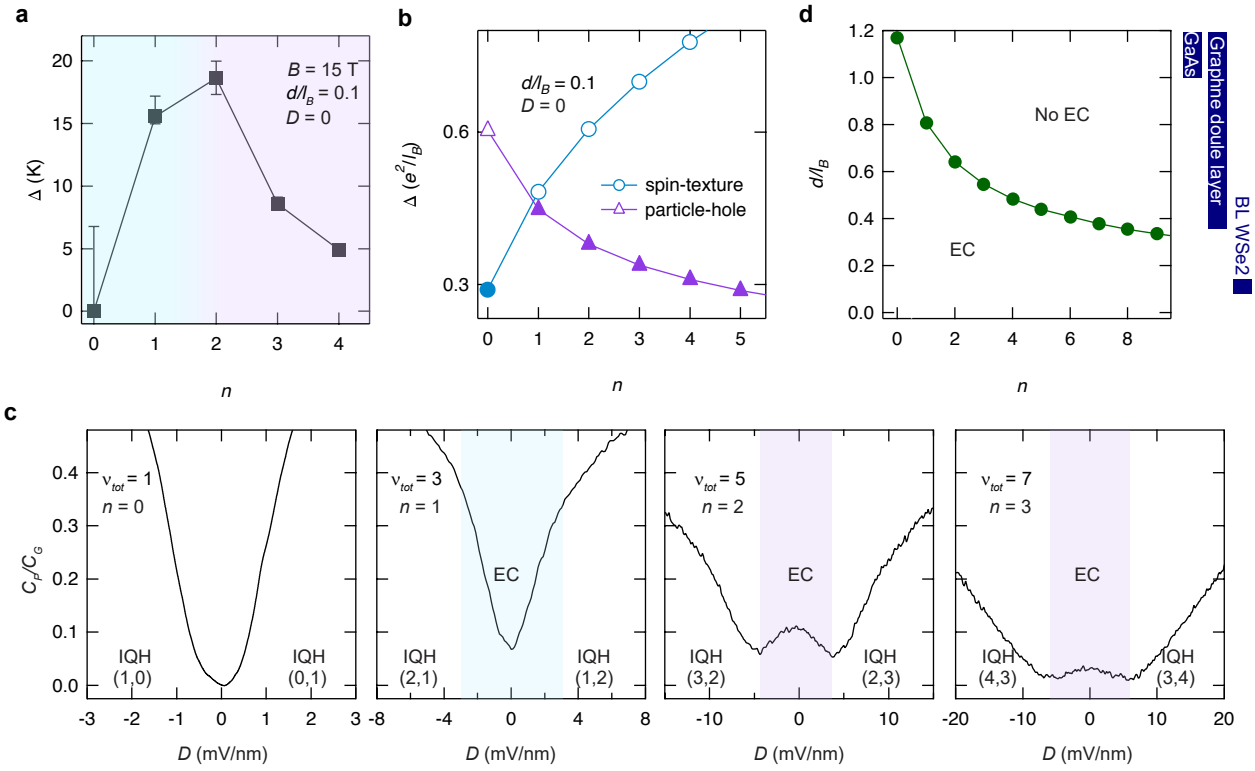

FIG. 4. **Different types of charged excitations for different LLs.** (a) Measured excitation gap when the layers are balanced ($D = 0$ and LLs in both layer are half-filled), at $B = 14.9$ T which corresponds to $d/l_B = 0.1$. Error bar for $n = 0$ reflects the uncertainty in distinguishing the EC gap at density balance from that at density imbalance or the IQH gap. Error bars for the rest represent the uncertainty in separating the stray capacitance or the polarizability contribution. Error bars are not shown when they are smaller than the symbol. (b) Theoretical estimate of charge gap values for layer balanced condition, for two types of excitations, at $d/l_B = 0.1$. The excitation energy of layer-pseudospin texture increases with n, while those for particle-hole excitations decreases with n. The filled markers stand for the lowest-energy excitations, which changes from one type to the other as n varies. (c) C_P/C_G as a function of D, at constant total filling factor $\nu_{tot} = 1, 3, 5, 7$, as marked, while the topmost LLs has orbital numbers $n = 0, 1, 2, 3$, respectively. A small background due to the polarizability contribution has been subtracted according to C_P at adjacent non-integer values. The shades highlight the D-range where the both layers are partially filled and charge is being transferred interlayer, while in the non-shaded regions both layers are at integer fillings as marked and the system exhibits an IQH gap. (d) Numerically calculated upper limit d/l_B for EC formation. Experimentally accessible ranges of d/l_B for different systems are marked on the right.

pears when the LLs in the two layers have matched orbital numbers (see SI.10 and SI.11). The consistency with theory further confirms the interpretation of the observed incompressible states as EC. In addition, our observation is consistent with previous experiments in graphene double-layers [8, 34] which demonstrated that spin and valley degrees of freedom are largely irrelevant in the formation of EC in the lowest LL. Intriguingly, the specific orbital number also plays a critical role in EC formation: EC formation is observed for $n = 1 - 6$, but is suppressed for $n = 0$, as shown by the dashed circles in Fig.3 (a) and (b) (see SI.5 and SI.6). This is precisely opposite to previous studies in double-layer systems with larger interlayer spacing [6–8], where the EC have only been observed for $n = 0$.

The critical role of the orbital number is further corroborated by the evolution of specific EC with magnetic field. This is displayed in Fig.3(c), which plots C_P versus the magnetic field and filling factor at the balanced condition $D = 0$. For $B < 10.5$ T, EC are clearly observed for $\nu_T = \nu_B = 4.5$, 5.5, and 6.5, but the state at $\nu_{B,T} = 5.5$ disappears abruptly above 10.5 T. This disappearance of EC coincides with a change in the orbital number from $n = 5$ to $n = 0$, as illustrated in Fig.3(d). The orbital number change is due to the rearrangement of the LLs with different spin indices, as illustrated in Fig.3(e). For a fixed filling factor, the carrier density scales linearly with the magnetic field, and at low densities, the g-factor which decides the Zeeman splitting between two spin branches are strongly enhanced [31]. Therefore, as B increases and the carrier density is raised above a threshold value, the active LLs at a fixed filling factor can switch from one spin to another and abruptly change orbital number to $n = 0$, leading to the disap-

pearance of EC (see SI.7).

To better understand the dependence of EC robustness on orbital number, we measure the excitation gap Δ by integrating $\partial\mu/\partial n$ over the gap at integer filling factors (see SI.8 for details). Fig.4(a) plots Δ *vs.* the orbital number n at $D = 0$, for $B = 14.9$ T: it exhibits a non-monotonic behavior with the maximum at $n = 2$. Tuning the orbital number modifies the single-particle electron wavefunction: as n increases, the wavefunctions spread out and have more nodes. In single-layer systems, at fractional fillings, this evolution often leads to different correlated ground states for different values of n. Here, although the ground state remains EC, the non-monotonic dependence of Δ on n stems from the change of the nature of low-energy charged excitations. The character of these excitations is more conveniently understood in the pseudospin picture. In this picture, electron states in the top (bottom) layer are viewed as pseudospin up (down), while the phase-coherent EC manifest macroscopically aligned pseudospin pointing in-plane [35]. On top of such a pseudospin ferromagnet ground state, one type of charged excitation is associated with a spatially extended pseudospin texture, known as meron-antimeron pair in the case of bilayer quantum Hall systems [35] (similar to skyrmions [36] in quantum Hall ferromagnets in a single-layer). As n increases, the energy of such excitations increases [37]. On the other hand, a conventional type of excitation, which represents a localised particle or hole, has an energy that decreases with n. As a result, a change in the nature of the lowest energy excitations is expected as n is varied. Fig.4(b) shows the theoretical estimate of the gap for the two types of excitations in a simple bilayer model without screening effects. The transition between two types of excitations occurs between $n = 0$ and $n = 1$, giving a non-monotonic dependence. This is qualitatively consistent with our data, except that in the model the gap maximum appears at $n = 1$, whereas the maximum appears at $n = 2$ in our measurement, suggesting that the pseudospin textured excitations also dominate at $n = 1$. The slight discrepancy with experimental data may be due to screening or disorder effects, which may lower the energy of pseudospin-texture excitations and shift the transition to higher n.

The different characteristics of the two kinds of excitations are also suggested by the density imbalance dependence, as shown in Fig.4(c). Here, we plot the penetration capacitance as a function of D, at a constant total filling factor $\nu_{tot} = 1, 3, 5, 7$, which are the four bottom circles in Fig.3(a) and (b), and correspond to LL orbital number $n = 0, 1, 2, 3$ respectively. The color shades in the right three panels illustrate the D-range where the individual layers host fractional filling factors, as suggested by the polarizability contribution at adjacent non-integer fillings. A larger C_P suggests a smaller electronic compressibility and a larger gap for charged excitations. Our data suggests that, for $n = 1$, the EC gap increases with D, and transitions smoothly into the IQH gap. In contrast, for $n = 2$ and 3, the EC gap decreases with D, and has a minimum before transitioning into the IQH state.

The distinct behavior of the two types of excitations is supported by our numerical calculations (see SI.12), which find that the meron-antimeron pairs have a sharp increase in gap with layer imbalance, while the particle-hole excitations show a flat response. While the pseudospin points in-plane for a density-balanced bilayer system, imbalancing the bilayer is equivalent to tilting the pseudospin out-of-plane, therefore the in-plane component of the spin-stiffness decreases [35]. For meron-antimeron pairs, the excitation energy has the main contribution from the meron and anti-meron self-energy, the sum of which increases with density imbalance. On the other hand, the particle-hole excitation energy is just the exchange energy, which is independent of the charge density imbalance. The decrease of the excitation gap with imbalance for $n = 2$ and 3 is not captured by our calculations and remains to be understood.

Finally, we remark that, in contrast to our bilayer WSe_2, in other quantum Hall double layer systems the EC has only been observed within the LL of orbital number $n = 0$. We find that, although numerical calculations suggests that EC could form in LLs of high orbital numbers, a smaller interlayer spacing is required for higher orbital numbers. As shown in Fig.4(d), the calculated critical interlayer spacing in units of the magnetic length, d_c/l_B, decreases sharply as a function of the orbital number n. The critical spacing d_c is estimated as the distance where the Goldstone mode goes soft at finite momentum, signaling the EC becoming unstable (see SI.11). On the right axis of Fig.4(d), we mark the experimentally accessible ranges of d/l_B for three different systems – GaAs double quantum wells, graphene double layers with BN barrier, and bilayer WSe_2. Our calculation suggests that the absence of EC in higher LLs in the first two systems is likely due to the large thickness of the intentional interlayer physical barrier (graphene also has the complication as the LL wavefunctions are mixture of simple harmonic oscillator wavefunctions). In contrast, the interlayer spacing in bilayer WSe_2 is set by the lattice constant in the vertical direction, which is only about 0.7 nm, and thus EC are expected to occur in higher LLs.

To conclude, our study demonstrates bilayer WSe_2 as a unique platform to access EC in the strong coupling limit, by exploiting the intrinsic spin-orbital coupling and stacking order in the host material. This designing principle could be further used in creating other quantum phases from layered van der Waals materials. For example, the interlayer hybridization could still be suppressed in, e.g., a twisted bilayer WSe_2 at a small angle deviation from the natural 2H-stacking. Combined with the flat-band originated from the moiré potential, such structures hosting strong electron-electron interactions and a well-defined layer degree freedom may set the basis for EC

at zero field and other exotic phases [38]. Finally, our study demonstrates EC composed from tunable single-particle orbital wavefunctions, and how such tunability could vary the properties of EC and the excitations on top of the ground state.

ACKNOWLEDGEMENTS

We thank Emanuel Tutuc for helpful discussions and William Coniglio and Bobby Pullum for help with experiments at the National High Magnetic Field Lab. This research is primarily supported by US Department of Energy (DE-SC0016703). Synthesis of WSe_2 (D.R.,B.K.,K.B.) was supported by the Columbia University Materials Science and Engineering Research Center (MRSEC), through NSF grants DMR-1420634 and DMR-2011738. A portion of this work was performed at the National High Magnetic Field Laboratory, which is supported by National Science Foundation Cooperative Agreement No. DMR-1157490 and the State of Florida. D.A. acknowledges support by the Swiss National Science Foundation and by the European Research Council (grant agreement No. 864597). Z.P. acknowledges support by the Leverhulme Trust Research Leadership Award RL-2019-015. K.W. and T.T. acknowledge support from the Elemental Strategy Initiative conducted by the MEXT, Japan (Grant Number JPMXP0112101001) and JSPS KAKENHI (Grant Numbers JP19H05790 and JP20H00354).

AUTHOR CONTRIBUTIONS STATEMENT

Q.S. fabricated the device, performed the capacitance measurements and analyzed the data. E.S. fabricated devices and performed transport measurements which complements the capacitance data. Z.P. and D.A.A. provided theoretical input and performed the numerical calculations. D.A.R. and B.K. grew the WSe_2 crystals under the supervision of J.H. and K.B.. K.W. and T.T. grew the hBN crystals. Q.S., C.R.D., J.H., Z.P. and D.A.A. wrote the manuscript with input from all authors.

COMPETING INTERESTS STATEMENT

The authors declare no competing interests.

* current affiliation: Physical Measurement Laboratory, National Institute of Standards and Technology, Gaithersburg, MD, USA; Department of Physics, Georgetown University, Washington, DC, USA.

[1] Blatt, J. M., Böer, K. W. & Brandt, W. Bose-einstein condensation of excitons. *Phys. Rev.* **126**, 1691–1692 (1962).

[2] Lozovik, Y. E. & Yudson, V. Feasibility of superfluidity of paired spatially separated electrons and holes; a new superconductivity mechanism. *JETP Lett.* **22**, 274–276 (1975).

[3] Snoke, D. Spontaneous bose coherence of excitons and polaritons. *Science* **298**, 1368–1372 (2002).

[4] Eisenstein, J. P. & MacDonald, A. H. Bose–einstein condensation of excitons in bilayer electron systems. *Nature* **432**, 691–694 (2004).

[5] Butov, L. V., Gossard, A. C. & Chemla, D. S. Macroscopically ordered state in an exciton system. *Nature* **418**, 751–754 (2002).

[6] Eisenstein, J. P. Exciton condensation in bilayer quantum hall systems. *Annu. Rev. Condens. Matter Phys.* **5**, 159 (2014).

[7] Liu, X., Taniguchi, T., Watanabe, K., Halperin, B. & Kim, P. Quantum hall drag of exciton condensate in graphene. *Nat. Phys.* **13**, 746–750 (2017).

[8] Li, J. I. A., Taniguchi, T., Watanabe, K., Hone, J. & Dean, C. R. Excitonic superfluid phase in double bilayer graphene. *Nat. Phys.* **13**, 751–755 (2017).

[9] Wang, Z. *et al.* Evidence of high-temperature exciton condensation in two-dimensional atomic double layers. *Nature* **574**, 76–80 (2019).

[10] Ma, L. *et al.* Strongly correlated excitonic insulator in atomic double layers (2021). arXiv:arXiv:2104.05066.

[11] Halperin, B. I. & Rice, T. M. Possible anomalies at a semimetal-semiconductor transistion. *Rev. Mod. Phys.* **40**, 755–766 (1968).

[12] Lu, Y. F. *et al.* Zero-gap semiconductor to excitonic insulator transition in ta2nise5. *Nature Communications* **8**, 14408 (2017).

[13] Kogar, A. *et al.* Signatures of exciton condensation in a transition metal dichalcogenide. *Science* **358**, 1314–1317 (2017).

[14] Li, Z. *et al.* Possible excitonic insulating phase in quantum-confined sb nanoflakes. *Nano Letters* **19**, 4960–4964 (2019). PMID: 31290676.

[15] Jia, Y. *et al.* Evidence for a monolayer excitonic insulator. *Nature Physics* (2021).

[16] Ataei, S. S., Varsano, D., Molinari, E. & Rontani, M. Evidence of ideal excitonic insulator in bulk mos2 under pressure. *Proceedings of the National Academy of Sciences* **118** (2021).

[17] Baldini, E. *et al.* The spontaneous symmetry breaking in ta_2nise_5 is structural in nature (2020). arXiv:arXiv:2007.02909.

[18] Mazza, G. *et al.* Nature of symmetry breaking at the excitonic insulator transition: ta_2nise_5. *Phys. Rev. Lett.* **124**, 197601 (2020).

[19] Butov, L. Condensation and pattern formation in cold exciton gases in coupled quantum wells. *Journal of Physics: Condensed Matter* **16**, R1577 (2004).

[20] Min, H., Bistritzer, R., Su, J.-J. & MacDonald, A. H. Room-temperature superfluidity in graphene bilayers. *Phys. Rev. B* **78**, 121401 (2008).

[21] Fogler, M. M., Butov, L. V. & Novoselov, K. S. High-temperature superfluidity with indirect excitons in van der waals heterostructures. *Nature Communications* **5**, 4555 EP – (2014). Article.

[22] Jauregui, L. A. *et al.* Electrical control of interlayer exciton dynamics in atomically thin heterostructures. *Science* **366**, 870–875 (2019).
[23] Nandi, D., Finck, A. D. K., Eisenstein, J. P., Pfeiffer, L. N. & West, K. W. Exciton condensation and perfect coulomb drag. *Nature* **488**, 481–484 (2012).
[24] Liu, X. *et al.* Crossover between strongly-coupled and weakly-coupled exciton superfluids (2020). arXiv:arXiv:2012.05916.
[25] Kim, Y., Moon, P., Watanabe, K., Taniguchi, T. & Smet, J. H. Odd integer quantum hall states with interlayer coherence in twisted bilayer graphene. *Nano Letters* **21**, 4249–4254 (2021).
[26] Gong, Z. *et al.* Magnetoelectric effects and valley-controlled spin quantum gates in transition metal dichalcogenide bilayers. *Nature Communications* **4**, 2053 (2013).
[27] Zeng, H. *et al.* Optical signature of symmetry variations and spin-valley coupling in atomically thin tungsten dichalcogenides. *Scientific Reports* **3**, 1608 (2013).
[28] Xu, X., Yao, W., Xiao, D. & Heinz, T. F. Spin and pseudospins in layered transition metal dichalcogenides. *Nature Physics* **10**, 343 (2014).
[29] Fallahazad, B. *et al.* Shubnikov–de haas oscillations of high-mobility holes in monolayer and bilayer wse_2: Landau level degeneracy, effective mass, and negative compressibility. *Phys. Rev. Lett.* **116**, 086601 (2016).
[30] Pisoni, R. *et al.* Absence of interlayer tunnel coupling of k-valley electrons in bilayer mos_2. *Phys. Rev. Lett.* **123**, 117702 (2019).
[31] Shi, Q. *et al.* Odd- and even-denominator fractional quantum hall states in monolayer wse2. *arXiv:1911.04428* (2019).
[32] Young, A. F. & Levitov, L. S. Capacitance of graphene bilayer as a probe of layer-specific properties. *Phys. Rev. B* **84**, 085441 (2011).
[33] Zibrov, A. A. *et al.* Tunable interacting composite fermion phases in a half-filled bilayer-graphene landau level. *Nature* **549**, 360–364 (2017).
[34] Li, J. I. A. *et al.* Pairing states of composite fermions in double-layer graphene. *Nature Physics* **15**, 898–903 (2019).
[35] Moon, K. *et al.* Spontaneous interlayer coherence in double-layer quantum hall systems: Charged vortices and kosterlitz-thouless phase transitions. *Phys. Rev. B* **51**, 5138–5170 (1995).
[36] Sondhi, S. L., Karlhede, A., Kivelson, S. A. & Rezayi, E. H. Skyrmions and the crossover from the integer to fractional quantum hall effect at small zeeman energies. *Phys. Rev. B* **47**, 16419–16426 (1993).
[37] Wu, X.-G. & Sondhi, S. L. Skyrmions in higher landau levels. *Phys. Rev. B* **51**, 14725–14728 (1995).
[38] Zhang, Y.-H., Sheng, D. N. & Vishwanath, A. Su(4) chiral spin liquid, exciton supersolid and electric detection in moiré bilayers (2021). arXiv:arXiv:2103.09825.

DATA AVAILABILITY

Experimental data relevant to figures in the main text and data of numerical calculations are available at https://doi.org/10.5281/zenodo.5866883. All other raw data are available from the corresponding author upon reasonable request.

METHOD

The heterostructure is assembled using the van der Waals dry transfer technique, and pre-patterned Pt electrodes are used for electrical contacts to bilayer WSe_2. Hexagonal boron nitride are used as the dielectric, and graphite or metal as top and bottom gates for bilayer WSe_2. The top gate was lithographically shaped so that its overlap with bottom gate covers only bilayer WSe_2, and the overlap defines the device area. In order to achieve good electrical contact, we use an additional contact gate on top to heavily dope the contact area, which is isolated from the top gate by Al_2O_3 dielectric. Data from a different device are shown in SI.9. Penetration capacitance was measured with an FHX35X high electron mobility transistor serving as a low-temperature amplifier, in a similar setup as in Ref. 31. Measurements were performed at $T = 0.3$ K unless otherwise specified.